



1 **Efficient droplet activation of ambient black carbon particles in sub-**  
2 **urban environment**

3 Ping Tian<sup>1</sup>, Dantong Liu<sup>2\*</sup>, Kang Hu<sup>2,3</sup>, Yangzhou Wu<sup>2,4</sup>, Mengyu Huang<sup>1,5</sup>, Hui He<sup>1,5</sup>, Jiujiang Sheng<sup>1,5</sup>,  
4 Chenjie Yu<sup>6</sup>, Dawei Hu<sup>7</sup>, Deping Ding<sup>1,5</sup>

5 <sup>1</sup> Beijing Key Laboratory of Cloud, Precipitation and Atmospheric Water Resources, Beijing Meteorological Service,  
6 Beijing, 100089, China

7 <sup>2</sup> Department of Atmospheric Sciences, School of Earth Sciences, Zhejiang University, Hangzhou 310058, China

8 <sup>3</sup> Jiangsu Collaborative Innovation Center of Atmospheric Environment and Equipment Technology, Jiangsu Key Laboratory  
9 of Atmospheric Environment Monitoring and Pollution Control, Nanjing University of Information Science & Technology,  
10 Nanjing, 210044, China

11 <sup>4</sup> College of Environmental Science and Engineering, Guilin University of Technology, Guilin, 541006, China

12 <sup>5</sup> Field Experiment Base of Cloud and Precipitation Research in North China, China Meteorological Administration, Beijing,  
13 100089, China

14 <sup>6</sup> Université Paris Cité and Univ Paris Est Créteil, CNRS, LISA, Paris, F-75013, France

15 <sup>7</sup> Department of Earth and Environment Sciences, University of Manchester, Manchester, UK.

16 *Corresponding to:* Dantong Liu ([dantongliu@zju.edu.cn](mailto:dantongliu@zju.edu.cn))

17



18 **Abstract**

19 The cloud condensation nuclei (CCN) activity of black carbon particles (BC) importantly determines their  
20 impacts on cloud microphysics and atmospheric lifetime. This process is crucially determined by the amount of  
21 more hygroscopic coating materials BC can acquire during aging process. It remains a challenge for ambient  
22 measurements to capture this process and link this with CCN activity of BC. Here by using coupled  
23 measurements of size-resolved number concentrations of CCN at configured water supersaturation (SS) and BC-  
24 containing particles (BCc), we are able to directly monitor the droplet activation diameter (D50) and activation  
25 fraction of BCc ( $F_{act,BC}$ ) in ambient environment. The number concentration of BCc was found to peak at  
26 diameter 180-210 nm after acquiring coatings, larger than that for all particles (50-150 nm). This led to that the  
27 initially smaller BC can be enlarged and become larger and more hygroscopic, even having higher CCN activities  
28 than other particles. The  $F_{act,BC}$  increased from 42% to 69% in number and from 67% to 85% in mass, as SS  
29 increased from 0.1% to 0.2%, but tended to reach a plateau when  $SS > 0.2\%$ . Notably,  $F_{act,BC}$  and D50 linearly  
30 correlated with equivalent photochemical age, at a rate of +2% per hour and -3nm per hour, respectively. The  
31 results suggest BCc from anthropogenic sources can readily serve as CCN at a relatively low SS, and over half of  
32 the BC population can be activated in a few hours. This means the surface-sourced BC can efficiently incorporate  
33 into clouds and may exert important indirect radiative impacts.

34 **Keywords:** black carbon; cloud condensation nuclei; droplet activation fraction; photochemical age

35



## 36 Introduction

37 Black carbon (BC), a significant anthropogenic pollutant, generate from the incomplete combustion of fossil fuels  
38 and profoundly influences the climate through direct (Ramanathan and Carmichael, 2008; Bond et al., 2013),  
39 indirect (Koch et al., 2011), and semi-direct (Koch and Del Genio, 2010) effects. The climate response to BC is  
40 sensitive to its lifetime (Hansen et al., 1997), which remains a considerable uncertainty in model studies due to  
41 spatial and temporal variations (Park et al., 2005; Koch et al., 2009; Lund et al., 2017).

42 Wet scavenging, the primary removal mechanism of atmospheric BC (Jacobson, 2010), that BC particles serve as  
43 cloud condensation nucleation (CCN) activated into the cloud droplets and removed through precipitation.  
44 Although freshly emitted BC particles are generally hydrophobic, they become more hygroscopic through  
45 atmospheric processing, acquiring soluble materials like sulfates, nitrates, and secondary organic aerosol  
46 compounds, or by coagulating with other particles (Dusek et al., 2006; Tritscher et al., 2011). The increased  
47 hygroscopicity enhances CCN activation efficiency of BC (Weingartner et al., 1995), yet there is significant  
48 variability in the literature regarding the degree to which BC serves as CCN (Wu et al., 2019; Rose et al., 2011),  
49 due to the diversity in properties of BC resulting from its various sources and atmospheric aging process  
50 (Henning et al., 2012; Dalirian et al., 2018).

51 The  $\kappa$ -Köhler theory (Petters and Kreidenweis, 2007), combined with the ZSR mixing rule (Pruppacher and Klett,  
52 1997; Henning et al., 2010), has been successful in characterizing the hygroscopicity of internally mixed BC,  
53 assuming a spherical core-shell structure. Chamber studies where the physic-chemical conditions and the initial  
54 emitted particles are well controlled indicate that the hygroscopicity of BC is determined by the fraction and  
55 hygroscopicity of the coating material (Snider et al., 2010; Friebel et al., 2019). A relatively thin soluble coating  
56 like 2nm corresponding to about 5% of the total volume for 250nm particles are enough to make hydrophobic BC  
57 CCN active under typical atmospheric supersaturation (Dalirian et al., 2018). The hygroscopic properties of the  
58 coating materials can vary significantly; notably, increase of the hygroscopicity of BC induced by secondary  
59 inorganic aerosols (e.g., ammonium nitrate) is more pronounced than that caused by organic aerosols (Kuwata et  
60 al., 2007; Liu et al., 2013). However, laboratory experiments often fail to replicate the complexity of atmospheric  
61 conditions, comprehensive field measurements are need to capture the real-time evolution of the CCN properties  
62 of BC.

63 Despite the advancements in understanding the physicochemical transformations of BC through field observation  
64 (Liu et al., 2017), quantifying its CCN activity in the ambient conditions remains challenging due to the  
65 variability in its sources, composition, mixing state, and atmospheric processes (Zhang et al., 2008). Direct field  
66 observations indicate that number fraction of 50%–90% BC can be activated into cloud or fog, dependent on  
67 actual ambient supersaturation (Motos et al., 2019a; Motos et al., 2019b;). More than 50% of BC mass can be  
68 removed through the wetting removing process during the transport from surface to planetary boundary layer  
69 (PBL), as evidenced in studies in East Asia polluted area (Kondo et al., 2016; Liu et al., 2020) in east Asian  
70 polluted area, but it's difficult to know true ambient supersaturation in the in-situ cloud observation. However,  
71 true ambient supersaturation is challenging to determine in in-situ cloud observations.

72 The hygroscopic of BC particles can be derived from the measured mixed state of BC by size resolved soot  
73 particle aerosol mass spectrometer (SP-AMS) (Onasch et al., 2012; Wu et al., 2019), and the hygroscopicity  
74 tandem differential mobility (HTDMA) instrument under sub saturation condition, however, only limited  
75 atmospheric CCN efficiency studies of BC particles were conducted under the water supersaturation condition.  
76 Continuous-flow cloud condensation nuclei counter (CCNC) can measure the CCN number concentration of the  
77 bulk aerosol under well-control supersaturation condition (Roberts and Nenes, 2005), but it cannot distinct how  
78 many parts of BC are activated as the number proportion of BC account for about 10% of the ambient aerosol.  
79 Recently, Hu et al. (2021a) developed an novel method to direct observe the number activation ratios of BC



80 under certain supersaturation, based on the size resolved CCNC and BC measurements, revealing potential  
81 overestimation of hygroscopicity of BC based on bulk chemical composition.

82 In this study, continuous observation of the CCN activation and hygroscopic properties of BC under water  
83 supersaturation (0.1%, 0.2%, and 0.3%) were conducted during springtime in a sub-urban site in Beijing. The  
84 variation of the hygroscopicity of BC during different pollution levels was investigated according to classification  
85 of four different air masses clusters. The equivalent photochemical age ( $t_{age}$ ), calculated based on the Proton-  
86 Transfer-Reactor Time-of-Flight Mass Spectrometer, was used to characterize the evolution of the CCN  
87 activation properties of BC under ambient atmospheric aging.

## 88 2. EXPERIMENTAL AND METHODS

### 89 2.1. Measurements site and Instruments Setup

90 The field campaign was conducted for more than 1 month from 29th Apr. to 2nd Jun. 2020 at Beijing Cloud  
91 Laboratory and Observational Utilities Deployment Base (CLOUD Base) (Tian et al., 2022), which is  
92 approximately 65Km to the northeast of the central Beijing, with the main local emissions are from industrial,  
93 traffic, and residential, which represent a typical sub-urban environment. Higher pollution condition at this site  
94 was correlate with pollutant regional transport from the west and south pollutant area, while clean condition was  
95 attribute to the pollutant dilution by the northwest clean air (Hu et al., 2022).

96 The instruments setup was shown in Figure 1a. The bulk and size-resolved physic-chemical and hygroscopicity  
97 properties of aerosol were simultaneously measured during the field campaign. A cyclone PM<sub>2.5</sub> cut-off inlet  
98 (Model: SCC1.829, BGI Inc., USA) was used to remove the coarse mode particles (larger than 2.5 $\mu$ m), and the  
99 air was dried by a Nafion tube before entering the instruments. In addition to particle measurement, volatile  
100 organic compounds (VOCs) were measured by a Proton-Transfer-Reactor Time-of-Flight Mass Spectrometer  
101 (PTR-TOF-MS 8000, Ionicon Analytik GmbH Innsbruck, Austria) (Fig. 1a).

### 102 2.2 Aerosol Chemical Components Measurements and Hygroscopic Growth Factor Calculation

103 The mass concentration of non-refractory submicron aerosol species including organic aerosol (OA), chloride  
104 ( $\text{Cl}^-$ ), ammonium ( $\text{NH}_4^+$ ), nitrate ( $\text{NO}_3^-$ ) and sulfate ( $\text{SO}_4^{2-}$ ) was measured by the Aerodyne high-resolution time-  
105 of-flight AMS (HR-ToF-AMS, Aerodyne Research Inc., USA). The principle and instruction of HR-ToF-AMS  
106 was already detailed in previous publications (Jayne et al., 2000; Drewnick et al., 2005). The HR-ToF-AMS was  
107 calibrated before and after the experiment, and relative ionization efficiencies of  $\text{NH}_4^+$  (4.0) and  $\text{SO}_4^{2-}$  (1.2) were  
108 calibrated using pure ammonium nitrate and ammonium sulfate, respectively, while default relative ionization  
109 efficiency values were used for OA (1.4),  $\text{NO}_3^-$  (1.1), and  $\text{Cl}^-$  (1.3) (Middlebrook et al., 2012).

110 The measurement of individual refractory black carbon (rBC)-containing particles (BCc) and BC-free particles  
111 (BCf) was conducted using the Single Particle Soot Photometer (SP2, DMT Inc., USA). The SP2 employs an  
112 intense  $\lambda=1064$  nm Nd:YAG laser to heat BCc until incandescence, with the mass and diameter ( $D_c$ ) of rBC  
113 quantified based on the intensity of the incandescence signal. Prior to the experiment, the incandescence signal  
114 was calibrated using Aquadag standards (Acheson Inc., USA) and was corrected for ambient BC using a factor of  
115 0.75 (Laborde et al., 2012).

116 The measurement of individual refractory BC (rBC)-containing particles (BCc) and BC-free particles (BCf) was  
117 conducted using the Single Particle Soot Photometer (SP2, DMT Inc., USA). The SP2 use intense 1064nm  
118 Nd:YAG laser beam to heat BCc to vaporize, with the mass and diameter ( $D_c$ ) of rBC quantified based on the  
119 intensity of the incandescence signal. The incandescence signal was calibrated using Aquadag standard (Acheson  
120 Inc. USA) and was corrected for ambient BC using a factor of 0.75 before the experiment (Laborde et al., 2012).  
121 Particles exhibiting only scattering signal were classified as BCf, with their diameters determined based on  
122 intensity of scattering signal, calibrated by polystyrene latex spheres (PSLs). Due to the distortion of the



123 scattering signal caused by the vaporization of the coating material of BCc, the leading edge only (LEO) fitting  
 124 method was employed to derive the entire size of BCc (Gao et al., 2007; Liu et al., 2014). As the optical diameter  
 125 of BCc is largely independent of the morphology of BCc, the measured optical diameter by SP2 is assumed to be  
 126 equal to the volume equivalent diameter ( $D_{ve}$ ) (Moteki et al., 2010; Hu et al., 2021b). Consequently, the relative  
 127 bulk volume of coating to BC ( $V_{coating}/V_{BC}$ ) was calculated as the cubic ratio of diameter of  $D_{ve}$  and  $D_c$  (Liu et al.,  
 128 2017):

$$129 \quad VR = \frac{V_{coating}}{V_{BC}} = \frac{\sum_i D_{ve}^3}{\sum_i D_c^3} - 1 \quad (1)$$

130 where  $D_{ve}$  is volume equivalent diameter of the entire BCc, and  $D_c$  is the rBC core diameter for the  $i^{th}$  single BCc ,  
 131 respectively.

132 The hygroscopic growth factor ( $\kappa$ ) which depend on the chemical properties (i.e. molecular weight, dissociate,  
 133 and osmotic coefficient, etc.) can be used to predict the activation properties of particles as CCN under certain  
 134 supersaturation (SS) (Petters and Kreidenweis, 2007). The hygroscopicity growth factor ( $\kappa$ ) for all-particles ( $\kappa_{all}$ )  
 135 were calculated applying Zdanovskii-Stokes-Robinson (ZRS) mixing rule for the volume contribution from  
 136 different chemical compositions (McDonald, 1953). The expression for  $\kappa_{all}$  is:

$$137 \quad \kappa_{all} = \sum_i \varepsilon_i \kappa_i \quad (2)$$

138 where  $\kappa_i$  and  $\varepsilon_i$  represents the hygroscopic growth factor and volume fraction for each chemical component (i.e.  
 139  $(NH_4)_2SO_4$ ,  $NH_4HSO_4$ ,  $NH_4NO_3$ , and BC etc.).

140 The  $\kappa$  of single BCc ( $\kappa_{BC}$ ) is depended on the volume fraction and  $\kappa$  of the coating material, and calculated as:

$$141 \quad \kappa_{BCc} = \kappa_{coating} \times \left( \frac{VR}{1+VR} \right) \quad (3)$$

142 where the  $\kappa_{coating}$  was chosen as the  $\kappa_{all}$  which also represent the average  $\kappa$  of particles, and  $V_{coating}/V_{BC}$  is  
 143 volume ratios of coating material over the BC, which reflect the coating thickness of BCc particles. The  $\kappa_{BC}$  was  
 144 test successfully to predict the activation of BCc as CCN in the field in-situ cloud observation (Motos et al.,  
 145 2019a).

### 146 2.3 Size Resolved CCN Activity of All-particles and BCc

147 Atmospheric polydisperse aerosols were classified into monodisperse particles at the outlet of a Differential  
 148 Mobility Analyser (DMA, Model: 3081, TSI Inc., USA). Particles of different mobility sizes were selected by  
 149 applying varying voltage to the DMA, maintaining a specific sheath flow rate (Knutson and Whitby, 1975).  
 150 Instead of employing the standard TSI Aerosol Instrument Manager control software, the DMA was governed by  
 151 custom-made software, enabling the selection of specific diameters and the control of residence time at those  
 152 diameters (Moore et al., 2010; Deng et al., 2011). A total of 29 mobility diameters ranging from 29 nm to 612 nm,  
 153 at logarithmic intervals, were chosen, and each diameter was maintained for 30 seconds. This time was selected  
 154 in consideration of the time lag (estimated to be less than 20s) between the instruments following the DMA (Fig.  
 155 1a). A complete size scan took approximately 15 minutes. The DMA's sheath and sample flow rates were  
 156 calibrated both before and after the experiment, and the mobility size selected by the DMA was validated using  
 157 PSLs.

158 The monodisperse number concentration of all condensation nuclei ( $[CN]$ ),  $[CCN]$ , and both  $[BCc]$  and  $[BCf]$  was  
 159 measured by a Condensation Particles Counter (CPC, Model 3772, TSI Inc., USA) with a flowrate of 0.30 L/min,  
 160 and a Cloud Condensation Nucleus counter (CCNc, DMT Inc., USA) with a flowrate of 0.50 L/min, and the other  
 161 Single Particle Soot Photometer (SP2, DMT Inc., USA) with a flowrate of 0.12 L/min, respectively (Fig. 1a).



162 Three SSs at 0.1%, 0.2%, 0.3% were set for the CCNc, and with an interval of 30 minutes, allowing two size  
 163 scans for each SS. The sample/sheath flowrate and also the SS of the CCNc were calibrated before and after the  
 164 experiment (Rose et al., 2008). Moreover, the monodisperse  $[CCN]$ ,  $[CN]$ , and  $[BCc]$  were corrected for multiple  
 165 charge effects, which performed from large particles (only have one negative charge) to smaller particles  
 166 according to charging probabilities for different mobility size (Wiedensohler, 1988).

167 The CCN activity of all-particles was determined based on the size resolved activation ratio ( $F_{act}$ ) ( $[CCN]/[CN]$ )  
 168 follow the method by Moore et al. (2010). This size resolved ratio,  $[CCN]/[CN]$ , reflect how many parts of CN  
 169 could serve as CCN can be directly measured by the CCNc and CPC with size scanning by the DMA.  $[CCN]/[CN]$   
 170 increase with the particle size, the ratio equals 1 at larger particle sizes (e.g., greater than 300 nm), whereas it  
 171 reduces to 0 at smaller sizes (e.g., 30 nm). The specific size at which the  $[CCN]/[CN]$  ratio reaches 0.5 is  
 172 identified as the activation diameter ( $D_{50}$ ). This critical value is generally derived through sigmoid fitting of the  
 173 size-resolved  $[CCN]/[CN]$  (Rose et al., 2008).

174 The CCN activated number concentration of BCc  $[BC_{act}]$  is discriminated from BCf and directly measured in this  
 175 study follow the method by Hu et al. (2021a), which compare the difference between the un-activated particle  
 176 number concentration ( $[CN_{unact}]$ ) and  $[BCc]$  to derived how many BCc are activate into CCN.  $[CN_{unact}]$  is derived  
 177 by subtracting the  $[CCN]$  from the total  $[CN]$ .  $[CN_{unact}]$  is zero at larger particle sizes, indicating that all particles,  
 178 including BCc, are activated. Conversely, when  $[CN_{unact}]$  equals the total  $[CN]$ , it signifies that none of the  
 179 particles are activated. It is well recognized activation of BCc into CCN is more challenging compare to that of  
 180 BCf at the same diameter, due to BCc's lower  $\kappa$  (Dusek et al., 2006; Bond et al., 2013). Only when the  $[CN_{unact}]$  is  
 181 smaller than  $[BCc]$ , it means some BCc have been activated into CCN, while  $[CN_{unact}]$  is zero, it means all BCc  
 182 are activated. So, the  $[BC_{act}]$  and activation ratios ( $F_{act,BC}$ ) of BCc are calculated as:

$$183 \quad [BC_{act}] = [BCc] - ([CN] - [CCN]) \quad (4)$$

$$184 \quad F_{act,BC} = ([BC_{act}]/[BCc]) \quad (5)$$

185  $[BC_{act}]$  is the difference between the  $[BCc]$  and  $[CN_{unact}]$ , and the  $F_{a,BC}$  is calculated by  $[BC_{act}]$  over the  $[BCc]$ .  
 186 When  $[CN_{unact}]$  is larger than  $[BCc]$  means none of BC could activate, the  $[BC_{act}]$  and  $F_{act,BC}$  is 0.

#### 187 2.4 Determination of the Photochemical Age

188 The PTR-TOF-AMS mass concentration measurement was calibrated by the  $CH_3COCH_4^+$  ( $m/z$  59.0490) and  
 189  $H_3O^+$  ( $m/z$  21.0226) following the procedures described by Bruns et al. (2016). The equivalent photochemical  
 190 age ( $t_{age}$ ), reflected the OH exposure dose of the air masses, was calculated as the change of toluene over benzene  
 191 concentration ratio due to their different reaction coefficient with OH, and expressed as:

$$192 \quad t_{age} = \frac{1}{[OH](k_{toluene} - k_{benzene})} \times \left[ \ln \left( \frac{[toluene]}{[benzene]} \right)_0 - \ln \left( \frac{[toluene]}{[benzene]} \right) \right] \quad (6)$$

193 where  $[OH]$  is the mean ambient OH concentration at  $2.5 \times 10^6$  molecule  $cm^{-3}$  during summer daytime in this  
 194 region (Yuan et al., 2012).  $k_{toluene}$  and  $k_{benzene}$  is the reaction rate with OH of toluene ( $5.63 \times 10^{-12}$   $cm^3$   
 195 molecule $^{-1}$  s $^{-1}$ ) and benzene ( $1.22 \times 10^{-12}$   $cm^3$  molecule $^{-1}$  s $^{-1}$ ), respectively.  $\left( \frac{[toluene]}{[benzene]} \right)_0$  is the ratio of freshly  
 196 emitted toluene and benzene which is assumed to be 3.3, and  $\frac{[toluene]}{[benzene]}$  is the ration of measured toluene and  
 197 benzene in the atmosphere. The calculation of  $t_{age}$  was only performed for the daytime to warrant it indicates the



198 photochemical process. The dataset of  $t_{age}$  in this study was already test successfully to obtain the reaction or  
199 production rates of secondary OA and VOCs (Wu et al., 2022).

## 200 2.5. Backward Trajectory Analysis

201 The potential source contribution to the target site was modelled by using Hybrid Single-Particle Lagrangian  
202 Integrated Trajectory Model (HYSPLIT) ensemble calculation with 3-hourly,  $1^\circ \times 1^\circ$  GDAS horizontal and  
203 vertical reanalysis wind field to retrieve backward 36-hour air mass to the target site, and air mass clusters came  
204 from four different directions were classified during the entire observation periods (Fig. 1b). Cluster 1 (C1) was  
205 from the southern polluted area, while C2-C4 were from the northern clean areas (Fig. 1b).

## 206 3. RESULTS AND DISCUSSION

### 207 3.1 Overview of the Aerosol Physical and Chemical Properties

208 Figure 2a-2d shows the time series of aerosol physical and chemical properties with the colour labels at the top  
209 represent different air masses influence periods, and the statistical comparison of aerosol properties between  
210 different air masses were show in Fig. 2e-2i. Consistent with previous studies, the aerosol physic-chemical  
211 properties were highly dependent on air masses (Tian et al., 2020; Zhao et al., 2020). Higher pollutant  
212 concentrations including  $PM_{10}$ , Sulphate, Nitrate, OA, and BC were observed during C1 period with air from  
213 southern part of North China Plain (NCP) (average  $PM_{10}$  value of  $33.2 \pm 16.4 \mu g m^{-3}$ ) (Fig. 2e and Fig. 2f), where  
214 contain high pollutant concentration due to the intensive emissions (Fig. 1b). When the air come from northern  
215 clean part of NCP during C3 and C4 period (Fig. 1b), lower pollutant concentrations were observed (average  $PM_{10}$   
216 value of  $10.4 \pm 5.8 \mu g m^{-3}$ ) (Fig. 2a and Fig. 2e), which suggest pollutants were diluted and dispersed during the  
217 fast transport process. Thus, C1 was estimated as polluted condition, while C3 and C4 was classified as clean  
218 environment. However, C2 came from the same direction as C4 but with less distances of transportation, which  
219 means smaller wind speeds to dilute the emissions, so the  $PM_{10}$  mass concentration ( $15.4 \pm 10.6 \mu g m^{-3}$ ) of C2 was  
220 higher than clean environment, but still one half lower than that of C1, and classified as light pollution condition  
221 (Fig. 2e).

222 During the transition from clean to pollution condition, the mass concentrations of all chemical components  
223 experienced substantial increase, as shown in Fig. 2a. Notably, the increase in inorganic aerosols (including  
224  $NH_4HSO_4$ ,  $(NH_4)_2SO_4$ , and  $NH_4NO_3$ ) was more pronounced than that of OA (Fig. 2b), which lead to lower/higher  
225 contribution of OA to all-particles during polluted/clean period (Fig. 2b and Fig. 2e). As  $\kappa_{all}$  is determined based  
226 on the volume fraction of OA and inorganic aerosol according to the ZSR internal mixing rule, this result distinct  
227  $\kappa_{all}$  characteristic for different airmasses influence periods (Fig. 2d and Fig. 2h).

### 228 3.2 The Hygroscopicity of BCc and All-particles

229 The  $\kappa_{all}$  (particles average hygroscopicity) varied from 0.13 to 0.45 with an average value of 0.29 during  
230 observation (Fig. 2d), the  $\kappa_{all}$  during C1 polluted period (average value of 0.38) was 1.5 times larger than that  
231 during C3/C4 clean period (average value 0.25) (Fig. 2h), this was attributed to the increased contribution of  
232 inorganic aerosol, known for their high hygroscopicity, under polluted condition.

233 The  $\kappa_{BC}$  is influenced by a combination of  $\kappa_{all}$  and the coating thickness (reflected by  $V_{coating}/V_{BC}$ ) (Eq. 3). The  
234  $V_{coating}/V_{BC}$  of BCc during C1 polluted period was  $4.9 \pm 4.2$ , which were about 3 - 5 times larger than that during  
235 C3/C4 clean period (Fig. 3c and Fig. 3g), implying thick coating of BCc under polluted condition. Due to both  
236 increase of  $V_{coating}/V_{BC}$  and  $\kappa_{all}$ , the  $\kappa_{BC}$  show similar variation characteristic as  $\kappa_{all}$  also with higher value under  
237 polluted condition (average value of 0.23), while lower value under clean condition (average value of 0.11) (Fig.  
238 2d and Fig. 2h).



239  $V_{\text{coating}}/V_{\text{BC}}$  exhibits a larger variation, ranging from 1.3 to 20, compared to  $\kappa_{\text{all}}$ , indicating that  $V_{\text{coating}}/V_{\text{BC}}$  has a  
 240 substantial influence on  $\kappa_{\text{BC}}$  (Fig. 2d). This can be evidenced by the maximum value of  $\kappa_{\text{BC}}$  correlates with that of  
 241  $V_{\text{coating}}/V_{\text{BC}}$  (Fig. 2c and Fig. 2d), and the divergence of the maximum values of  $\kappa_{\text{all}}$  and  $\kappa_{\text{BC}}$  (Fig. 2d). The coating  
 242 of BCc is formed through by the photo-chemistry of VOCs precursors during the atmosphere aging process,  
 243 which is determined by VOCs precursors and also aging time. Comparing to the clean clusters C3 and C4, the air  
 244 mass movement of C1 was much slower, combined with passing the highest pollution level region, the slowly  
 245 transported air mass from the polluted southern region was characterized with a longer transport time than other  
 246 air mass clusters (Fig. 1b). As expected, the observation of PTR-ToF-MS shows higher VOCs values and also the  
 247 longer  $t_{\text{age}}$  during C1 polluted condition (Fig. S2). Figure 2i show that the  $t_{\text{age}}$  during C1 polluted period (13h) was  
 248 about one times larger than that during C3/C4 clean period (9h), this reflected the air during polluted period was  
 249 more aged.

250 Figure 3 shows diurnal variation of PM<sub>1</sub>, BC mass concentration, OA fraction,  $V_{\text{coating}}/V_{\text{BC}}$ ,  $\kappa_{\text{all}}$  and  $\kappa_{\text{BC}}$  for the  
 251 different air masses respectively. More pronounced diurnal patterns were found during the C3/C4 clean period, as  
 252 the fast-moving clean air masses dilute the pollutant and were mainly influenced by local emissions, however,  
 253 regional transport and secondary aerosol formation influence the diurnal pattern during C1 and C2 period (Fig.  
 254 2a). For chemical inert BC particles, clear BC mass peaking at morning and afternoon rush-hour (marked as grey  
 255 bar) (Fig. 3b) was observed which is typical time period of heavy traffic with nascent BC emitted, but C1 period  
 256 showed a continuous transport and increased BC mass loading throughout the midday, even when developed  
 257 planetary boundary layer (PBL) dilute the pollutants.

258 Fresher BCc showed lowest  $V_{\text{coating}}/V_{\text{BC}}$  during the morning rush-hours, and within a few hours the  $V_{\text{coating}}/V_{\text{BC}}$   
 259 quickly increase and peak at noon when solar radiation was strongest for all-time period (Fig. 3d). The increase  
 260 during midday was in consistent with the OA fraction (Fig. 3c), which suggested that the acquire coating of BC  
 261 particles might be secondary OA through the photochemical oxidation, inconsistent with recently studies (Cui et  
 262 al., 2022; Wu et al., 2019). As enhanced OA fraction at noon due to photochemical SOA formation (Fig. 3c),  
 263 result a lower value of  $\kappa_{\text{all}}$  during noontime (Fig. 3e).  $\kappa_{\text{BC}}$  is more influenced by the  $V_{\text{coating}}/V_{\text{BC}}$ , the  $\kappa_{\text{BC}}$  was found  
 264 increase after morning rush-hours due to the increase of coating on BC.

### 265 3.3. The CCN Activation Properties of All-particles and BCc

#### 266 3.3.1 Determining the D50 of BCc

267 The measurement of the activation properties of all-particles and BCc into CCN was discussed in Sec. 2.3.2.  
 268 Figure 4 illustrates a representative example of size-resolved activation of all-particle and BCc at SS = 0.1% and  
 269 0.3% respectively. Activation commences for all-particles when  $[CCN]$  is greater than 0 (depicted by blue lines),  
 270 while BCc (indicated by black lines) begins to activate when the  $[CN_{\text{unact}}]$  (represent by green lines) falls below  
 271 that of  $[BCc]$  (Fig. 4).  $[BC_{\text{act}}]$  (denoted by the grey shadow) can be derived using Equation 4, and the size-  
 272 resolved  $F_{\text{act,BC}}$  can be calculated in accordance with Equation 5. It can be seen that with the increase of particle  
 273 size, BCc started to get activated at 0.19 $\mu\text{m}$  (0.13 $\mu\text{m}$ ) at SS=0.1% (0.3%), which is higher than all-particle by 44%  
 274 (46%), the higher D50 of BCc also indicates that the lower  $\kappa_{\text{BC}}$  than  $\kappa_{\text{all}}$ .

275 We would like to emphasize that the principal uncertainty in the method employed stems from the assumption  
 276 regarding the lower  $\kappa$  for BC compared to other particles. The assumption was consistent with concurrent  
 277 theoretical understanding, pure BC was hydrophobic ( $\kappa_{\text{BC}}=0$ ), though the  $\kappa_{\text{BC}}$  increase by acquire hygroscopic  
 278 coating through atmospheric aging (Grimonprez et al., 2018; Weingartner et al., 1997), the  $\kappa_{\text{BC}}$  remains lower  
 279 than other components under the same atmospheric oxidation process based on ZSR volume mixing rule. Most  
 280 importantly, even though some internally mixing BCc activate into CCN previous to other chemical components,  
 281 the results here was underestimated the  $[BC_{\text{act}}]$  and  $F_{\text{act,BC}}$ , so the CCN activity of BCc derived through this  
 282 method could represent the low bound of the atmospheric BCc.





### 283 3.3.2 D50 of BCc and All-particles

284 Figure 5 illustrate the temporal evolution of size distribution of BCc, CN and CCN, respectively. The [CCN]  
285 increase during polluted condition due to the increase BCc and all-particles concentration, and the [CCN]  
286 is mainly contributed by all-particles (Fig. 5c). The derived D50 for BCc and all-particles under water SS at 0.1%,  
287 0.2%, and 0.3% is shown as lines in Fig. 5a-c for the temporal evolution, and mean value is shown as vertical  
288 dash lines in Fig. 5d. The mean D50 of BCc particles (0.17 $\mu$ m, 0.13 $\mu$ m, and 0.12 $\mu$ m under SS= 0.1%, 0.2%, and  
289 0.3%) was approximate 1.4 times larger than that of all-particles (0.11 $\mu$ m, 0.08 $\mu$ m, and 0.07 $\mu$ m under SS= 0.1%,  
290 0.2%, and 0.3%) (Fig. 5), which was expected from  $\kappa$ -Köhler theory (Petters and Kreidenweis, 2007) that  
291 lower/higher D50 means the higher/lower  $\kappa$ . The higher D50 of BCc also reflected lower  $\kappa$  and BCc should be  
292 activated in the last order.

293 Large variation of D50 of BCc and all-particles was also found for different air massed (Fig. 5), the D50 of all-  
294 particles (0.13 $\mu$ m  $\pm$  0.01 $\mu$ m) and BCc (0.20 $\mu$ m  $\pm$  0.01 $\mu$ m) during C1 polluted period was lower that (0.15 $\mu$ m  $\pm$   
295 0.02 $\mu$ m) and (0.23 $\mu$ m  $\pm$  0.02 $\mu$ m) during C3/C4 clean period. This is also inconsistent with the variation of  $\kappa_{all}$   
296 and  $\kappa_{BC}$  (discussed in 3.2), suggested the more inorganic fraction increase  $\kappa_{all}$  and the thick coating increase the  
297  $\kappa_{BC}$  during the polluted condition.

298 Figure 6a and 6b illustrate the diurnal variation of D50 of all-particles and BCc under SS=0.10%, the other two  
299 SSs at 0.20% and 0.30% are shown in Fig. S3 and Fig. S4. The diurnal variation was more pronounce under clean  
300 period (i.e. C3+C4), when local emission dominate the pollution sources. Higher D50 of all-particles and BCc  
301 was found during the rush-hours when more primary hydrophobic OA and fresh external mixed BCc emitted.  
302 The D50 of all-particles and BCc will decrease after photochemistry oxidation secondary OA formation and  
303 coating on BCc which was also in consistent with that of  $\kappa_{all}$  and  $\kappa_{BC}$  (Fig. 3).

### 304 3.3.3 Droplet Activation Fraction of BCc and All-particles

305 Figure 5d shows the averaged size distribution of BCc, CN and CCN under three SSs for different periods  
306 classified by air mass clusters (C1-C4). Notably BCc had consistently larger peak size than all-particles for all air  
307 masses. For example, BCc peak from 185 to 210nm, which was about 2-4 times larger than that of all-particles,  
308 which peaked from 58 to 115nm. The more polluted air masses (C1 and C2) had larger peak size of BCc and CN  
309 than cleaner air masses (C3 and C4), because of the condensation process during the polluted episode when gases  
310 heavily partitioned to aerosol phase and enlarged particle size.

311 Though the BC core size is smaller, after attaching on larger particles the overall coated size is even significantly  
312 larger than BCf. This means in the typical sub-urban environment, BC had been significantly associated with  
313 non-BC substance through condensation and coagulation process (Yu et al., 2022), and the bare BC without  
314 containing non-BC substance had taken a less proportion and most BCc had been enlarged during the aging  
315 process. This is consistent with previous studies that BC was associated with larger aerodynamic size than BCf  
316 (Pan et al., 2019; Wang et al., 2021). Previous studies also observed rapid aging of BC in a few hours in urban  
317 environment (Peng et al., 2016).

318 Figure 6d and 6e show the diurnal variations  $F_{act}$  (in number and mass) for all-particles and BCc under SS=0.1%.  
319 The other two SSs at 0.2% and 0.3% are shown in Figure S2 and Figure S3. With SS increase from 0.1% to 0.2%,  
320 the number  $F_{act,BC}$  and  $F_{act,all}$  increased from 42% $\pm$ 15% to 69% $\pm$ 15% and from 30% $\pm$ 15% to 51% $\pm$ 19%. Figure 6f  
321 show the statistical  $F_{act}$  results compare for different air masses. the number  $F_{act,BC}$  increased from 30% to 53%  
322 under SS=0.1% (Fig. 6f) with the pollution increase from C3/C4 to C1. The mass  $F_{act,BC}$  show similar variation  
323 characteristic as the number  $F_{act,BC}$ , which increase from 58 % to 76 % under SS=0.1% from C3/C4 to C1 period  
324 (Fig. 6f), and from 81% to 89% and from 87% to 91%, under SS at 0.2% and 0.3%, respectively. BCc acquires  
325 thicker hygroscopic coating through longer atmospheric aging time during the long range regional transport C1  
326 polluted period, the hygroscopic coating not only increase  $\kappa_{BC}$  and lead to a lower D50, also increasing the BCc



327 size. The decrease of D50 and increase of particle size both led to an increase of  $F_{act}$ . The  $F_{act,BC}$  mainly depended  
 328 on the  $V_{coating}/V_{BC}$ , as the D50 and size of BCc was dependent on  $V_{coating}/V_{BC}$ . The diurnal variation also show  
 329 lowest  $F_{act,BC}$  during rush hours due to lower  $V_{coating}/V_{BC}$ , and increased in the daytime with increased  $V_{coating}/V_{BC}$   
 330 (Fig. 6e).

331 The number  $F_{act,BC}$  was always higher than  $F_{act,all}$  under all SSs (Fig. 6, Fig. S2 and Fig. S3), due to the size of  
 332 BCc is larger than all-particles. The mass  $F_{act,BC}$  was about 1.61 higher than in number, compared with about 2.88  
 333 difference of mass and number  $F_{act}$  for all-particles. This is also caused by the larger size distribution of BCc than  
 334 all-particle. The large portion of all-particles in small size drives the number  $F_{act}$  to be lower than BCc. Although  
 335 D50 of BC is higher, the larger size distribution of BCc than all-particles means BCc can have a higher droplet  
 336 removing efficiency than BCf.

337 The large  $F_{act,BC}$  than BCf particles, and thickly coated BCc have preference in CCN activation was also observed  
 338 through cloud residues observation at a mountain site in south China (Fu et al., 2022). The measured  $F_{act}$  was  
 339 generally consistent with experiment conducted in a South China mega city using the same method (Hu et al.,  
 340 2021a), but are higher than cloud residues observation in China (Zhang et al., 2017), which reported an average  
 341 value 33% of the mass  $F_{act,BC}$  and number  $F_{act}$  of BCc (all-particle) ranged in 5%-45% (7%-60%). We attribute  
 342 the difference to unknow ambient SS for the cloud, which have great influence on the  $F_{act,BC}$ . According to  
 343 previous cloud residues observation at Jungfraujoch, the number  $F_{act,BC}$  increase from 50% to 80% when SS  
 344 increase from 0.21% to 0.50% (Motos et al., 2019a; Hammer et al., 2014). The ambient SS show large variation  
 345 can be range from 0.01% to 2.00% (Hammer et al., 2014), however, it is hardly to direct observe the SS from the  
 346 field observation. Through this method the number and mass  $F_{act,BC}$  activated into droplets can be quantitatively  
 347 investigate under certain ambient SS condition, thus the results here provide a reference to investigate the lifetime  
 348 of BCc.

### 349 3.4. Time Scale for the Evolution of CCN Activity of BCc

350 The temporal evolution of parameters related to CCN activity including  $\kappa$ , D50 and  $F_{act}$  against photochemical  
 351 age ( $t_{age}$ ) for BCc and all-particles are shown in Fig. 7. It shows that the aging time ( $t_{age}$ ) can well explain the  
 352 variation of all parameters for BCc and all-particles with a linear function ( $R^2 > 0.4$ ).

353 The volume ratio of coating over rBC ( $V_{coating}/V_{BC}$ ) showed an increase rate of  $0.14 \text{ h}^{-1}$  (Fig. S4), and can be fitted  
 354 as:

$$355 \quad V_{coating}/V_{BC} = 0.55 + 0.14 \cdot t_{age} \quad (7)$$

356 This results in a linear increase rate for the hygroscopicity parameter,  $\kappa_{BC}$  showed a linear rate of  $0.09 \text{ h}^{-1}$  ((Fig.  
 357 7a, 7b, and 7c)) at all SSs, can be fitted as:

$$358 \quad \kappa_{BC} = 0.09 + 0.01 \cdot t_{age} \quad (8)$$

359 In addition,  $\kappa_{BC}$  also follow a linear function with  $t_{age}$  as:

$$360 \quad \kappa_{all} = 0.16 + 0.014 \cdot t_{age} \quad (9)$$

361 This means the  $\kappa$  for the large proportion of non-BC is enhanced after aging due to enhanced formation of  
 362 inorganic salt and secondary organic aerosols (Wu et al., 2022). The results show it will take about 24 and 10  
 363 hours to reach the global mean  $\kappa$  of 0.27-0.30 (Pringle et al., 2010) for BCc and all particles, respectively.

364 The aging scale of a few hours observed here is generally consistent with previously measured BC aging  
 365 influenced by anthropogenic pollution, such as an aircraft measurement (Moteki et al., 2012) which observed the  
 366 conversion time scale of BC was a few hours under polluted environment. The results were also comparable with  
 367 previous chamber studies which investigated the evolution of BC (Tritscher et al., 2011; Lambe et al., 2015;



368 Peng et al., 2017), the increase rate of  $\kappa_{BC}$  ( $0.01\text{h}^{-1}$ ) in this study was similar, but the initial  $\kappa_{BC}$  here (0.08-0.26)  
369 was higher than the fresh combustion soot as used in their results (0-0.12). These consistently showed a few  
370 hours tended to be a typical aging time scale to convert appreciable amount of initially hydrophobic BC to be  
371 hydrophilic, hereby CCN active. The exact time scale may according to pollution level, such as a higher  
372 concentration of gas precursors and favoured meteorological condition may promote the growth rate of  
373 hygroscopic substances on BC.

374 Correspondingly, the D50 of BCc particles and all-particles decreased with  $t_{age}$ , with a rate of  $-3\text{ nm h}^{-1}$  and  $-3\text{ nm}$   
375  $\text{h}^{-1}$ (Fig. 7d),  $-1\text{ nm h}^{-1}$  and  $-2\text{ nm h}^{-1}$  (Fig. 7e), and  $-0.5\text{ nm h}^{-1}$  and  $-2\text{ nm h}^{-1}$  (Fig. 7f) under SS = 0.10%, 0.20%,  
376 and 0.30%, respectively. The results are summarized in Table 1.

377 The number activation fraction  $F_{act,all}$  and  $F_{act,BC}$  also show linear correlation with  $t_{age}$ . A notable higher CCN  
378 activation fraction was observed for BCc than all particles at the same  $t_{age}$ , this was attributed to the larger coated  
379 size of BCc than other non-BC particles (Fig. 5). This difference between BCc and other particles was reduced at  
380 longer  $t_{age}$  because the sufficient aging time had allowed all particles to grow to similar large sizes.

381 After 8 hours of aging,  $F_{act,BC}$  increased from 35% to 63% as SS rose from 0.1% to 0.2%, and then increase from  
382 63% to 77% as SS increase from 0.2% to 0.3%. This illustrates a notable increase in  $F_{act,BC}$  from SS=0.1% to  
383 0.20%, but a less significantly changed  $F_{act,BC}$  from SS=0.2% to 0.3%. Furthermore, the rate increase of  $F_{act,BC}$   
384 with  $t_{age}$  was  $2\% \text{ h}^{-1}$  at SS=0.10% (Fig.7g), which was twice as large as at SS=0.2% ( $1\% \text{ h}^{-1}$ ) (Fig. 7h) and 0.3%  
385 ( $1\% \text{ h}^{-1}$ ) (Fig. 7i). This indicated that the activation of BCc was more sensitive at lower SS ( $<0.2\%$ ), but may  
386 reach a plateau when SS $>0.2\%$ . This is because the activation diameter at this typical SS range was close to the  
387 mode size of BCc number distribution (Fig. 5d), and a small increase of SS will cause a considerable change of  
388 fraction which is larger than the activation diameter. The SS range from 0.1% to 0.2% is for the typical formation  
389 of fog and stratiform thin clouds (Hammer et al., 2014).

#### 390 4. Conclusion

391 In this study, we conduct directly measurements of the droplet activation of BC-containing particles under water  
392 supersaturation conditions in a sub-urban environment. Both the hygroscopicity and CCN activation diameters  
393 reveal that the hygroscopicity of all-particles and BCc concurrently increase with polluted levels, primarily  
394 governed by the amounts of coating. As pollution intensifies, the volume ratio of coating over rBC increases from  
395 1.8 to 4.7, causing the hygroscopicity of BCc to increase from 0.11 to 0.23. The increase of coating not only  
396 increase BCc's hygroscopicity but also shifts these particles to larger sizes, significantly enhance their CCN  
397 activity. The number activated fraction of BCc was 42% under SS at 0.1%, higher than the 30% activation of all  
398 particles. Despite the lower hygroscopicity, the elevated activation fraction of BCc can be attributed to their  
399 larger size compared to all particles. It was also found that the number activated fraction of BCc was more  
400 sensitive in the SS range from 0.1% to 0.2%, a typical range for fog and stratiform thin clouds formation. This  
401 means a small increase of SS even for the environment with relatively low moisture and weak updraft the BC can  
402 be activated. Considering these clouds have a lower precipitation rate, BC in these clouds may have more  
403 persistent indirect radiative impacts.

404 Furthermore, we successfully parameterized the evolution of hygroscopicity and CCN activation characteristics  
405 of BCc and all particles in relation to equivalent photochemical age. The hygroscopicity of BCc was found  
406 positive linearly correlated with aging time with a rate of  $0.01\text{ h}^{-1}$ , and the activation diameter negative correlated  
407 with a rate of  $1-3\text{ nm h}^{-1}$ . Within 10 hours, 65% of BCc activated under SS=0.2% in this typical sub-urban  
408 environment, this is in line with a wide range of recent ambient studies that BC can be half activated under



409 SS=0.1-0.2%. This means these BCc may be efficiently incorporated into clouds by serving as CCN. This aging  
410 process by acquiring more hygroscopic substances of BC may be particularly important under polluted  
411 environment, where the condensation and coagulation processes intensively occurred. The results here thus  
412 provide direct evidence of efficient droplet activation of BCc, and the aging scale associated with their CCN  
413 activation can be used as a reference to validate the regional models regarding aerosol-cloud interactions of BC.

414 **Data availability.** All data in this paper are available from the authors upon request (tianping@bj.cma.gov.cn).

415 **Competing interests.** At least one of the (co-)authors is a member of the editorial board of Atmospheric  
416 Chemistry and Physics.

417 **Author contribution.** D. D., and M. H. led and designed the study; P. T. and D. L. designed the study, set up the  
418 experiment, analysed the data, and wrote the paper. K. H. and Y. W. conducted the field observation and  
419 contributed the data analysis. H. H. and J. S performed the calibration of the instruments. C. Y. and D. H  
420 contributed to scientific discussion.

421 **Acknowledgment.** This research was supported by the National key Research and Development Program of  
422 China (2023YFC3007600), and National Natural Science Foundation of China (42175116, 41975180, 42275087).

423



424 **Reference**

- 425 Bond, T. C., Doherty, S. J., Fahey, D. W., Forster, P. M., Bernsten, T., DeAngelo, B. J., Flanner, M. G., Ghan, S.,  
426 Kärcher, B., Koch, D., Kinne, S., Kondo, Y., Quinn, P. K., Sarofim, M. C., Schultz, M. G., Schulz, M.,  
427 Venkataraman, C., Zhang, H., Zhang, S., Bellouin, N., Guttikunda, S. K., Hopke, P. K., Jacobson, M. Z., Kaiser,  
428 J. W., Klimont, Z., Lohmann, U., Schwarz, J. P., Shindell, D., Storelvmo, T., Warren, S. G., and Zender, C. S.:  
429 Bounding the role of black carbon in the climate system: A scientific assessment, *J. Geophys. Res. Atmos.*, 118,  
430 5380-5552, 10.1002/jgrd.50171, 2013.
- 431 Bruns, E. A., El Haddad, I., Slowik, J. G., Kilic, D., Klein, F., Baltensperger, U., and Prevot, A. S.: Identification  
432 of significant precursor gases of secondary organic aerosols from residential wood combustion, *Sci Rep*, 6, 27881,  
433 10.1038/srep27881, 2016.
- 434 Cui, S., Huang, D. D., Wu, Y., Wang, J., Shen, F., Xian, J., Zhang, Y., Wang, H., Huang, C., Liao, H., and Ge, X.:  
435 Chemical properties, sources and size-resolved hygroscopicity of submicron black-carbon-containing aerosols in  
436 urban Shanghai, *Atmos. Chem. Phys.*, 22, 8073-8096, 10.5194/acp-22-8073-2022, 2022.
- 437 Dalirian, M., Ylisirniö, A., Buchholz, A., Schlesinger, D., Ström, J., Virtanen, A., and Riipinen, I.: Cloud droplet  
438 activation of black carbon particles coated with organic compounds of varying solubility, *Atmos. Chem. Phys.*,  
439 18, 12477-12489, 10.5194/acp-18-12477-2018, 2018.
- 440 Deng, Z. Z., Zhao, C. S., Ma, N., Liu, P. F., Ran, L., Xu, W. Y., Chen, J., Liang, Z., Liang, S., Huang, M. Y., Ma,  
441 X. C., Zhang, Q., Quan, J. N., Yan, P., Henning, S., Mildenerberger, K., Sommerhage, E., Schäfer, M., Stratmann,  
442 F., and Wiedensohler, A.: Size-resolved and bulk activation properties of aerosols in the North China Plain,  
443 *Atmos. Chem. Phys.*, 11, 3835-3846, 10.5194/acp-11-3835-2011, 2011.
- 444 Drewnick, F., Hings, S. S., DeCarlo, P., Jayne, J. T., Gonin, M., Fuhrer, K., Weimer, S., Jimenez, J. L.,  
445 Demerjian, K. L., Borrmann, S., and Worsnop, D. R.: A New Time-of-Flight Aerosol Mass Spectrometer (TOF-  
446 AMS)—Instrument Description and First Field Deployment, *Aerosol Sci. Technol.*, 39, 637-658,  
447 10.1080/02786820500182040, 2005.
- 448 Dusek, U., Reischl, G. P., and Hitznerberger, R.: CCN activation of pure and coated carbon black particles,  
449 *Environ. Sci. Technol.*, 40, 1223-1230, 2006.
- 450 Friebel, F., Lobo, P., Neubauer, D., Lohmann, U., Drossaert van Dusseldorp, S., Mühlhofer, E., and Mensah, A.  
451 A.: Impact of isolated atmospheric aging processes on the cloud condensation nuclei activation of soot particles,  
452 *Atmos. Chem. Phys.*, 19, 15545-15567, 10.5194/acp-19-15545-2019, 2019.
- 453 Fu, Y., Peng, X., Sun, W., Hu, X., Wang, D., Yang, Y., Guo, Z., Wang, Y., Zhang, G., Zhu, J., Ou, J., Shi, Z.,  
454 Wang, X., and Bi, X.: Impact of Cloud Process in the Mixing State and Microphysical Properties of Soot  
455 Particles: Implications in Light Absorption Enhancement, *J. Geophys. Res. Atmos.*, 127, 10.1029/2022jd037169,  
456 2022.
- 457 Gao, R. S., Schwarz, J. P., Kelly, K. K., Fahey, D. W., Watts, L. A., Thompson, T. L., Spackman, J. R., Slowik, J.  
458 G., Cross, E. S., Han, J. H., Davidovits, P., Onasch, T. B., and Worsnop, D. R.: A Novel Method for Estimating  
459 Light-Scattering Properties of Soot Aerosols Using a Modified Single-Particle Soot Photometer, *Aerosol Sci.*  
460 *Technol.*, 41, 125-135, 10.1080/02786820601118398, 2007.
- 461 Grimonprez, S., Faccinnetto, A., Batut, S., Wu, J., Desgroux, P., and Petitprez, D.: Cloud condensation nuclei  
462 from the activation with ozone of soot particles sampled from a kerosene diffusion flame, *Aerosol Sci. Technol.*,  
463 52, 814-827, 10.1080/02786826.2018.1472367, 2018.
- 464 Hammer, E., Bukowiecki, N., Gysel, M., Jurányi, Z., Hoyle, C. R., Vogt, R., Baltensperger, U., and Weingartner,  
465 E.: Investigation of the effective peak supersaturation for liquid-phase clouds at the high-alpine site Jungfraujoch,  
466 Switzerland (3580 m a.s.l.), *Atmos. Chem. Phys.*, 14, 1123-1139, 10.5194/acp-14-1123-2014, 2014.
- 467 Hansen, J., Sato, M., and Ruedy, R.: Radiative forcing and climate response, *J. Geophys. Res. Atmos.*, 102, 6831-  
468 6864, 10.1029/96jd03436, 1997.
- 469 Henning, S., Ziese, M., Kiselev, A., Saathoff, H., Möhler, O., Mentel, T. F., Buchholz, A., Spindler, C., Michaud,



- 470 V., Monier, M., Sellegri, K., and Stratmann, F.: Hygroscopic growth and droplet activation of soot particles:  
471 uncoated, succinic or sulfuric acid coated, *Atmos. Chem. Phys.*, 12, 4525-4537, 10.5194/acp-12-4525-2012, 2012.  
472 Henning, S., Wex, H., Hennig, T., Kiselev, A., Snider, J. R., Rose, D., Dusek, U., Frank, G. P., Pöschl, U.,  
473 Kristensson, A., Bilde, M., Tillmann, R., Kiendler-Scharr, A., Mentel, T. F., Walter, S., Schneider, J., Wennrich,  
474 C., and Stratmann, F.: Soluble mass, hygroscopic growth, and droplet activation of coated soot particles during  
475 LACIS Experiment in November (LExNo), *J. Geophys. Res.*, 115, 10.1029/2009jd012626, 2010.  
476 Hu, D., Liu, D., Kong, S., Zhao, D., Wu, Y., Li, S., Ding, S., Zheng, S., Cheng, Y., Hu, K., Deng, Z., Wu, Y.,  
477 Tian, P., Liu, Q., Huang, M., and Ding, D.: Direct Quantification of Droplet Activation of Ambient Black Carbon  
478 Under Water Supersaturation, *J. Geophys. Res. Atmos.*, 126, 10.1029/2021jd034649, 2021a.  
479 Hu, K., Liu, D., Tian, P., Wu, Y., Deng, Z., Wu, Y., Zhao, D., Li, R., Sheng, J., Huang, M., Ding, D., Li, W.,  
480 Wang, Y., and Wu, Y.: Measurements of the Diversity of Shape and Mixing State for Ambient Black Carbon  
481 Particles, *Geophys. Res. Lett.*, 48, 10.1029/2021gl094522, 2021b.  
482 Hu, K., Liu, D., Tian, P., Wu, Y., Li, S., Zhao, D., Li, R., Sheng, J., Huang, M., Ding, D., Liu, Q., Jiang, X., Li,  
483 Q., and Tao, J.: Identifying the Fraction of Core–Shell Black Carbon Particles in a Complex Mixture to Constrain  
484 the Absorption Enhancement by Coatings, *Environmental Science & Technology Letters*, 9, 272-279,  
485 10.1021/acs.estlett.2c00060, 2022.  
486 Jacobson, M. Z.: Short-term effects of controlling fossil-fuel soot, biofuel soot and gases, and methane on climate,  
487 Arctic ice, and air pollution health, *J. Geophys. Res.*, 115, 10.1029/2009jd013795, 2010.  
488 Jayne, J. T., Leard, D. C., Zhang, X., Davidovits, P., Smith, K. A., Kolb, C. E., and Worsnop, D. R.:  
489 Development of an Aerosol Mass Spectrometer for Size and Composition Analysis of Submicron Particles,  
490 *Aerosol Sci. Technol.*, 33, 49-70, 10.1080/027868200410840, 2000.  
491 Knutson, E. O. and Whitby, K. T.: Aerosol classification by electric mobility: Apparatus, Theory, and  
492 Applications, *Aerosol Sci.*, 6, 443, 1975.  
493 Koch, D. and Del Genio, A. D.: Black carbon semi-direct effects on cloud cover: review and synthesis, *Atmos.*  
494 *Chem. Phys.*, 10, 7685-7696, 10.5194/acp-10-7685-2010, 2010.  
495 Koch, D., Balkanski, Y., Bauer, S. E., Easter, R. C., Ferrachat, S., Ghan, S. J., Hoose, C., Iversen, T., Kirkevåg,  
496 A., Kristjansson, J. E., Liu, X., Lohmann, U., Menon, S., Quaas, J., Schulz, M., Seland, Ø., Takemura, T., and  
497 Yan, N.: Soot microphysical effects on liquid clouds, a multi-model investigation, *Atmos. Chem. Phys.*, 11,  
498 1051-1064, 10.5194/acp-11-1051-2011, 2011.  
499 Koch, D., Schulz, M., Kinne, S., McNaughton, C., Spackman, J. R., Balkanski, Y., Bauer, S., Bernsten, T., Bond,  
500 T., Boucher, O., Chin, M., Clarke, A., Luca, N. D., Dentener, F., Diehl, T., Dubovik, O., Easter, R., Fahey, D. W.,  
501 Feichter, J., Fillmore, D., Freitag, S., Ghan, S., Ginoux, P., Gong, S., Horowitz, L., Iversen, T., Kirkevåg, A.,  
502 Kilmont, Z., Kondo, Y., Krol, M., Liu, X., Miller, R., Montanaro, V., Moteki, N., Myhre, G., Penner, J. E.,  
503 Perlwiz, J., Pitari, G., Reddy, S., Sahu, L., Sakamoto, H., Schuster, G., Schwarz, J. P., Seland, Ø., Siter, P.,  
504 Takegawa, N., Takemura, T., Textor, C., van Aardenne, J. A., and Zhao, Y.: Evaluation of black carbon  
505 estimations in global aerosol models, *Atmos. Chem. Phys.*, 9, 9001-9026, 2009.  
506 Kondo, Y., Moteki, N., Oshima, N., Ohata, S., Koike, M., Shibano, Y., Takegawa, N., and Kita, K.: Effects of  
507 wet deposition on the abundance and size distribution of black carbon in East Asia, *J. Geophys. Res. Atmos.*, 121,  
508 4691-4712, 10.1002/2015jd024479, 2016.  
509 Kuwata, M., Kondo, Y., Mochida, M., Takegawa, N., and Kawamura, K.: Dependence of CCN activity of less  
510 volatile particles on the amount of coating observed in Tokyo, *J. Geophys. Res.*, 112, 10.1029/2006jd007758,  
511 2007.  
512 Laborde, M., Mertes, P., Zieger, P., Dommen, J., Baltensperger, U., and Gysel, M.: Sensitivity of the Single  
513 Particle Soot Photometer to different black carbon types, *Atmos. Meas. Tech.*, 5, 1031-1043, 10.5194/amt-5-  
514 1031-2012, 2012.  
515 Lambe, A. T., Ahern, A. T., Wright, J. P., Croasdale, D. R., Davidovits, P., and Onasch, T. B.: Oxidative aging



- 516 and cloud condensation nuclei activation of laboratory combustion soot, *J. Aerosol Res.*, 79, 31-39,  
517 10.1016/j.jaerosci.2014.10.001, 2015.
- 518 Liu, D., Allan, J., Whitehead, J., Young, D., Flynn, M., Coe, H., McFiggans, G., Fleming, Z. L., and Bandy, B.:  
519 Ambient black carbon particle hygroscopic properties controlled by mixing state and composition, *Atmos. Chem.*  
520 *Phys.*, 13, 2015-2029, 10.5194/acp-13-2015-2013, 2013.
- 521 Liu, D., Allan, J. D., Young, D. E., Coe, H., Beddows, D., Fleming, Z. L., Flynn, M. J., Gallagher, M. W.,  
522 Harrison, R. M., Lee, J., Prevot, A. S. H., Taylor, J. W., Yin, J., Williams, P. I., and Zotter, P.: Size distribution,  
523 mixing state and source apportionment of black carbon aerosol in London during wintertime, *Atmos. Chem.*  
524 *Phys.*, 14, 10061-10084, 10.5194/acp-14-10061-2014, 2014.
- 525 Liu, D., Ding, S., Zhao, D., Hu, K., Yu, C., Hu, D., Wu, Y., Zhou, C., Tian, P., Liu, Q., Wu, Y., Zhang, J., Kong,  
526 S., Huang, M., and Ding, D.: Black Carbon Emission and Wet Scavenging From Surface to the Top of Boundary  
527 Layer Over Beijing Region, *J. Geophys. Res. Atmos.*, 125, 10.1029/2020jd033096, 2020.
- 528 Liu, D., Whitehead, J., Alfarra, M. R., Reyes-Villegas, E., Spracklen, Dominick V., Reddington, Carly L., Kong,  
529 S., Williams, Paul I., Ting, Y.-C., Haslett, S., Taylor, Jonathan W., Flynn, Michael J., Morgan, William T.,  
530 McFiggans, G., Coe, H., and Allan, James D.: Black-carbon absorption enhancement in the atmosphere  
531 determined by particle mixing state, *Nature Geoscience*, 10, 184-188, 10.1038/ngeo2901, 2017.
- 532 Lund, M. T., Berntsen, T. K., and Samset, B. H.: Sensitivity of black carbon concentrations and climate impact to  
533 aging and scavenging in OsloCTM2–M7, *Atmos. Chem. Phys.*, 17, 6003-6022, 10.5194/acp-17-6003-2017, 2017.
- 534 McDonald, J. E.: Erroneous Cloud-Physics Applications of Raoult's Law, *Journal of Meteorology*, 10, 68-70,  
535 1953.
- 536 Middlebrook, A. M., Bahreini, R., Jimenez, J. L., and Canagaratna, M. R.: Evaluation of Composition-Dependent  
537 Collection Efficiencies for the Aerodyne Aerosol Mass Spectrometer using Field Data, *Aerosol Sci. Technol.*, 46,  
538 258-271, 10.1080/02786826.2011.620041, 2012.
- 539 Moore, R. H., Nenes, A., and Medina, J.: Scanning Mobility CCN Analysis—A Method for Fast Measurements  
540 of Size-Resolved CCN Distributions and Activation Kinetics, *Aerosol Sci. Technol.*, 44, 861-871,  
541 10.1080/02786826.2010.498715, 2010.
- 542 Moteki, N., Kondo, Y., and Nakamura, S.-i.: Method to measure refractive indices of small nonspherical particles:  
543 Application to black carbon particles, *J. Aerosol Res.*, 41, 513-521, 10.1016/j.jaerosci.2010.02.013, 2010.
- 544 Moteki, N., Kondo, Y., Oshima, N., Takegawa, N., Koike, M., Kita, K., Matsui, H., and Kajino, M.: Size  
545 dependence of wet removal of black carbon aerosols during transport from the boundary layer to the free  
546 troposphere, *Geophys. Res. Lett.*, 39, n/a-n/a, 10.1029/2012gl052034, 2012.
- 547 Motos, G., Schmale, J., Corbin, J. C., Zanatta, M., Baltensperger, U., and Gysel-Beer, M.: Droplet activation  
548 behaviour of atmospheric black carbon particles in fog as a function of their size and mixing state, *Atmos. Chem.*  
549 *Phys.*, 19, 2183-2207, 10.5194/acp-19-2183-2019, 2019a.
- 550 Motos, G., Schmale, J., Corbin, J. C., Modini, R. L., Karlen, N., Bertò, M., Baltensperger, U., and Gysel-Beer,  
551 M.: Cloud droplet activation properties and scavenged fraction of black carbon in liquid-phase clouds at the high-  
552 alpine research station Jungfraujoch (3580&thinsp;m&thinsp;a.s.l.), *Atmos. Chem. Phys.*, 19, 3833-3855,  
553 10.5194/acp-19-3833-2019, 2019b.
- 554 Onasch, T. B., Trimborn, A., Fortner, E. C., Jayne, J. T., Kok, G. L., Williams, L. R., Davidovits, P., and  
555 Worsnop, D. R.: Soot Particle Aerosol Mass Spectrometer: Development, Validation, and Initial Application,  
556 *Aerosol Sci. Technol.*, 46, 804-817, 10.1080/02786826.2012.663948, 2012.
- 557 Pan, X., Liu, H., Wu, Y., Tian, Y., Sun, Y., Xie, C., Liu, X., Cheng, T., and Wang, Z.: Dynamic shape factor and  
558 mixing state of refractory black carbon particles in winter in Beijing using an AAC-DMA-SP2 tandem system,  
559 *Atmos. Chem. Phys. Discuss*, 10.5194/acp-2019-433, 2019.
- 560 Park, R. J., Jacob, D. J., Palmer, P. I., Clarke, A. D., Weber, R. J., Zondlo, M. A., Eisele, F. L., Bandy, A. R.,  
561 Thornton, D. C., Sachse, G. W., and Bond, T. C.: Export efficiency of black carbon aerosol in continental



- 562 outflow: Global implications, *J. Geophys. Res. Atmos.*, 110, 10.1029/2004jd005432, 2005.
- 563 Peng, J., Hu, M., Guo, S., Du, Z., Shang, D., Zheng, J., Zheng, J., Zeng, L., Shao, M., Wu, Y., Collins, D., and  
564 Zhang, R.: Ageing and hygroscopicity variation of black carbon particles in Beijing measured by a quasi-  
565 atmospheric aerosol evolution study (QUALITY) chamber, *Atmos. Chem. Phys.*, 17, 10333-10348, 10.5194/acp-  
566 17-10333-2017, 2017.
- 567 Peng, J., Hu, M., Guo, S., Du, Z., Zheng, J., Shang, D., Zamora, M. L., Zeng, L., Shao, M., Wu, Y., Zheng, J.,  
568 Wang, Y., Glen, C. R., Collins, D., Molina, M. J., and Zhang, R.: Markedly enhanced absorption and direct  
569 radiative forcing of black carbon under polluted urban environments, *Proc Natl Acad Sci U S A*, 113, 4266-4271,  
570 2016.
- 571 Petters, M. D. and Kreidenweis, S. M.: A single parameter representation of hygroscopic growth and cloud  
572 condensation nucleus activity, *Atmos. Chem. Phys.*, 7, 1961-1971, 2007.
- 573 Pringle, K. J., Tost, H., Pozzer, A., Pöschl, U., and Lelieveld, J.: Global distribution of the effective aerosol  
574 hygroscopicity parameter for CCN activation, *Atmos. Chem. Phys.*, 10, 5241-5255, 10.5194/acp-10-5241-2010,  
575 2010.
- 576 Pruppacher, H. R. and Klett, J. D.: *Microphysics of Cloud and Precipitation*, Kluwer Academic Publishers,  
577 Dordrecht 1997.
- 578 Ramanathan, V. and Carmichael, G.: Global and regional climate changes due to black carbon, *Nature*  
579 *Geoscience*, 1, 221-227, 2008.
- 580 Roberts, G. C. and Nenes, A.: A Continuous-Flow Streamwise Thermal-Gradient CCN Chamber for Atmospheric  
581 Measurements, *Aerosol Sci. Technol.*, 39, 206-221, 10.1080/027868290913988, 2005.
- 582 Rose, D., Gunthe, S. S., Mikhailov, E., Frank, G. P., Dusek, U., Andreae, M. O., and Pöschl, U.: Calibration and  
583 measurement uncertainties of a continuous-flow cloud condensation nuclei counter (DMT-CCNC): CCN  
584 activation of ammonium sulfate and sodium chloride aerosol particles in theory and experiment, *Atmos. Chem.*  
585 *Phys.*, 8, 1153-1179, 2008.
- 586 Rose, D., Gunthe, S. S., Su, H., Garland, R. M., Yang, H., Berghof, M., Cheng, Y. F., Wehner, B., Achtert, P.,  
587 Nowak, A., Wiedensohler, A., Takegawa, N., Kondo, Y., Hu, M., Zhang, Y., Andreae, M. O., and Pöschl, U.:  
588 Cloud condensation nuclei in polluted air and biomass burning smoke near the mega-city Guangzhou, China –  
589 Part 2: Size-resolved aerosol chemical composition, diurnal cycles, and externally mixed weakly CCN-active  
590 soot particles, *Atmos. Chem. Phys.*, 11, 2817-2836, 10.5194/acp-11-2817-2011, 2011.
- 591 Snider, J. R., Wex, H., Rose, D., Kristensson, A., Stratmann, F., Hennig, T., Henning, S., Kiselev, A., Bilde, M.,  
592 Burkhardt, M., Dusek, U., Frank, G. P., Kiendler-Scharr, A., Mentel, T. F., Petters, M. D., and Pöschl, U.:  
593 Intercomparison of cloud condensation nuclei and hygroscopic fraction measurements: Coated soot particles  
594 investigated during the LACIS Experiment in November (LExNo), *J. Geophys. Res.*, 115, 10.1029/2009jd012618,  
595 2010.
- 596 Tian, P., Liu, D., Zhao, D., Yu, C., Liu, Q., Huang, M., Deng, Z., Ran, L., Wu, Y., Ding, S., Hu, K., Zhao, G.,  
597 Zhao, C., and Ding, D.: In situ vertical characteristics of optical properties and heating rates of aerosol over  
598 Beijing, *Atmos. Chem. Phys.*, 20, 2603-2622, 10.5194/acp-20-2603-2020, 2020.
- 599 Tian, P., Liu, D., Bi, K., Huang, M., Wu, Y., Hu, K., Li, R., He, H., Ding, D., Hu, Y., Liu, Q., Zhao, D., Qiu, Y.,  
600 Kong, S., and Xue, H.: Evidence for Anthropogenic Organic Aerosols Contributing to Ice Nucleation, *Geophys.*  
601 *Res. Lett.*, 49, 10.1029/2022gl099990, 2022.
- 602 Tritscher, T., Jurányi, Z., Martin, M., Chirico, R., Gysel, M., Heringa, M. F., DeCarlo, P. F., Sierau, B., Prévôt, A.  
603 S. H., Weingartner, E., and Baltensperger, U.: Changes of hygroscopicity and morphology during ageing of  
604 diesel soot, *Environmental Research Letters*, 6, 034026, 10.1088/1748-9326/6/3/034026, 2011.
- 605 Wang, S., Zhou, K., Lu, X., Chen, H., Yang, F., Li, Q., Yang, X., and Wang, X.: Measurement of Density and  
606 Shape for Single Black Carbon Aerosols in a Heavily Polluted Urban Area, *Aerosol. Air. Qual. Res.*, 21, 210162,  
607 10.4209/aaqr.210162, 2021.





- 608 Weingartner, E., Baltensperger, U., and Burtscher, H.: Growth and Structural Change of Combustion Aerosols at  
609 High Relative Humidity, *Environ. Sci. Technol*, 29, 2982-2986, 1995.
- 610 Weingartner, E., Burtscher, H., and Baltensperger, U.: Hygroscopic properties of carbon and diesel soot particles,  
611 *Atmos. Environ.*, 31, 2311-2327, 1997.
- 612 Wiedensohler, A.: An approximation of the bipolar charge distribution for particles in the submicron size range, *J.*  
613 *Aerosol Sci*, 19, 387-389, 1988.
- 614 Wu, Y., Liu, D., Wang, J., Shen, F., Chen, Y., Cui, S., Ge, S., Wu, Y., Chen, M., and Ge, X.: Characterization of  
615 Size-Resolved Hygroscopicity of Black Carbon-Containing Particle in Urban Environment, *Environ Sci Technol*,  
616 53, 14212-14221, 10.1021/acs.est.9b05546, 2019.
- 617 Wu, Y., Liu, D., Tian, P., Sheng, J., Liu, Q., Li, R., Hu, K., Jiang, X., Li, S., Bi, K., Zhao, D., Huang, M., Ding,  
618 D., and Wang, J.: Tracing the Formation of Secondary Aerosols Influenced by Solar Radiation and Relative  
619 Humidity in Suburban Environment, *J. Geophys. Res. Atmos.*, 127, 10.1029/2022jd036913, 2022.
- 620 Yu, C., Liu, D., Hu, K., Tian, P., Wu, Y., Zhao, D., Wu, H., Hu, D., Guo, W., Li, Q., Huang, M., Ding, D., and  
621 Allan, J. D.: Aerodynamic size-resolved composition and cloud condensation nuclei properties of aerosols in a  
622 Beijing suburban region, *Atmos. Chem. Phys.*, 22, 4375-4391, 10.5194/acp-22-4375-2022, 2022.
- 623 Yuan, B., Shao, M., de Gouw, J., Parrish, D. D., Lu, S., Wang, M., Zeng, L., Zhang, Q., Song, Y., Zhang, J., and  
624 Hu, M.: Volatile organic compounds (VOCs) in urban air: How chemistry affects the interpretation of positive  
625 matrix factorization (PMF) analysis, *J. Geophys. Res. Atmos.*, 117, D24302, 10.1029/2012jd018236, 2012.
- 626 Zhang, G., Lin, Q., Peng, L., Bi, X., Chen, D., Li, M., Li, L., Brechtel, F. J., Chen, J., Yan, W., Wang, X., Peng,  
627 P., amp, apos, an, Sheng, G., and Zhou, Z.: The single-particle mixing state and cloud scavenging of black carbon:  
628 a case study at a high-altitude mountain site in southern China, *Atmos. Chem. Phys.*, 17, 14975-14985,  
629 10.5194/acp-17-14975-2017, 2017.
- 630 Zhang, R., Khalizov, A. F., Pagels, J., Zhang, D., Xue, H., and McMurry, P. H.: Variability in morphology,  
631 hygroscopicity, and optical properties of soot aerosols during atmospheric processing, *Proc. Natl. Acad. Sci. USA*,  
632 105, 10291-10296, 10.1073/pnas.0804860105, 2008.
- 633 Zhao, D., Liu, D., Yu, C., Tian, P., Hu, D., Zhou, W., Ding, S., Hu, K., Sun, Z., Huang, M., Huang, Y., Yang, Y.,  
634 Wang, F., Sheng, J., Liu, Q., Kong, S., Li, X., He, H., and Ding, D.: Vertical evolution of black carbon  
635 characteristics and heating rate during a haze event in Beijing winter, *The Science of the total environment*, 709,  
636 136251, 10.1016/j.scitotenv.2019.136251, 2020.

637



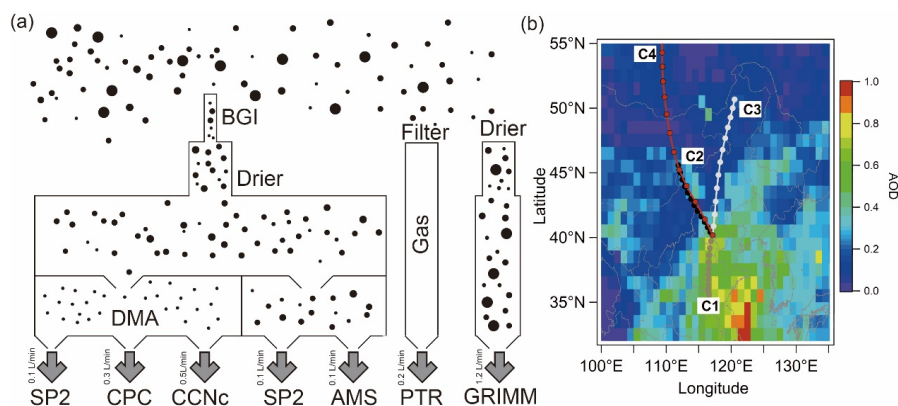
638 Table 1. A summary of linear fitting results for activation diameter ( $D_{50}$ ) and activation fraction ( $F_{act}$ ) of all  
 639 particles and BCc-containing particles.  
 640

Initial, Slope	Activation diameter ( $D_{50}$ )		Activation fraction ( $F_{act}$ )	
	All particles	BC-containing particles	All particles	BC-containing particles
SS=0.1%	170nm, -3nm h <sup>-1</sup>	240nm, -3nm h <sup>-1</sup>	4%, 2% h <sup>-1</sup>	19%, 2% h <sup>-1</sup>
SS=0.2%	120nm, -2nm h <sup>-1</sup>	170nm, -1nm h <sup>-1</sup>	18%, 0.3%h <sup>-1</sup>	55%, 0.1% h <sup>-1</sup>
SS=0.3%	100nm, -2nm h <sup>-1</sup>	150nm, -0.5nm h <sup>-1</sup>	26%, 0.3% h <sup>-1</sup>	69%, 0.1% h <sup>-1</sup>

641



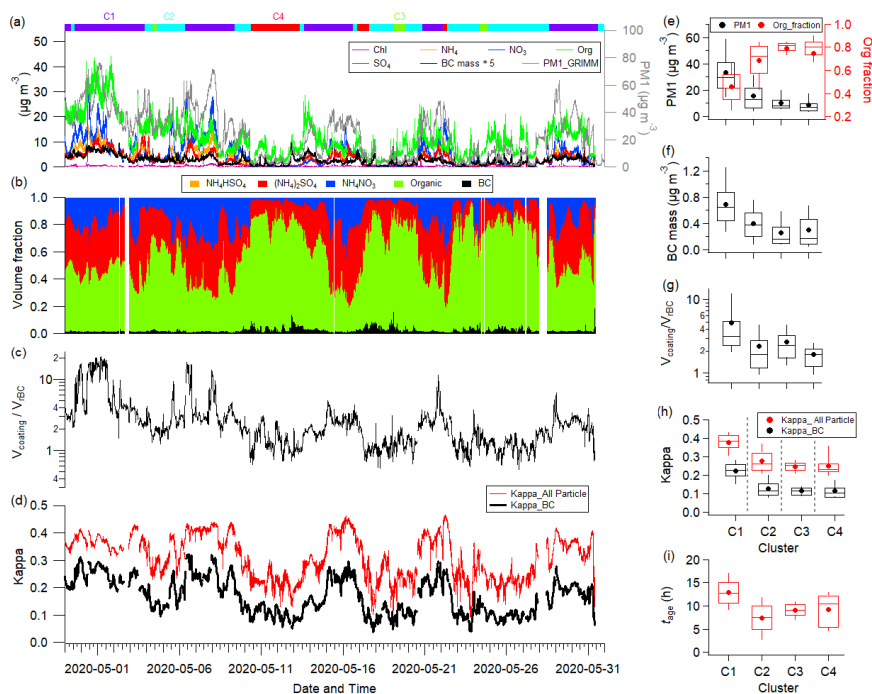
642 **Figures and captions**



643

644 **Figure 1.** Schematic of the experiment. a) Experimental setup showing aerosols are sampled through a  $PM_{2.5}$   
645 impactor following a drier. Mono-dispersed aerosol was measured downstream of a differential mobility analyser  
646 (DMA), including SP2, CPC and CCNc, and additional line measure the poly-dispersed aerosols with SP2 and  
647 HR-ToF-AMS. All sizes of dried aerosol are measured by a GRIMM, and the VOC concentration was measured  
648 by a PTR-TOF-AMS. b) Mean aerosol optical depth (AOD) during the experimental month, with three lines  
649 showing the clustered 36h backward trajectories initialized from the experimental site with each markers  
650 denoting 6h transport time.

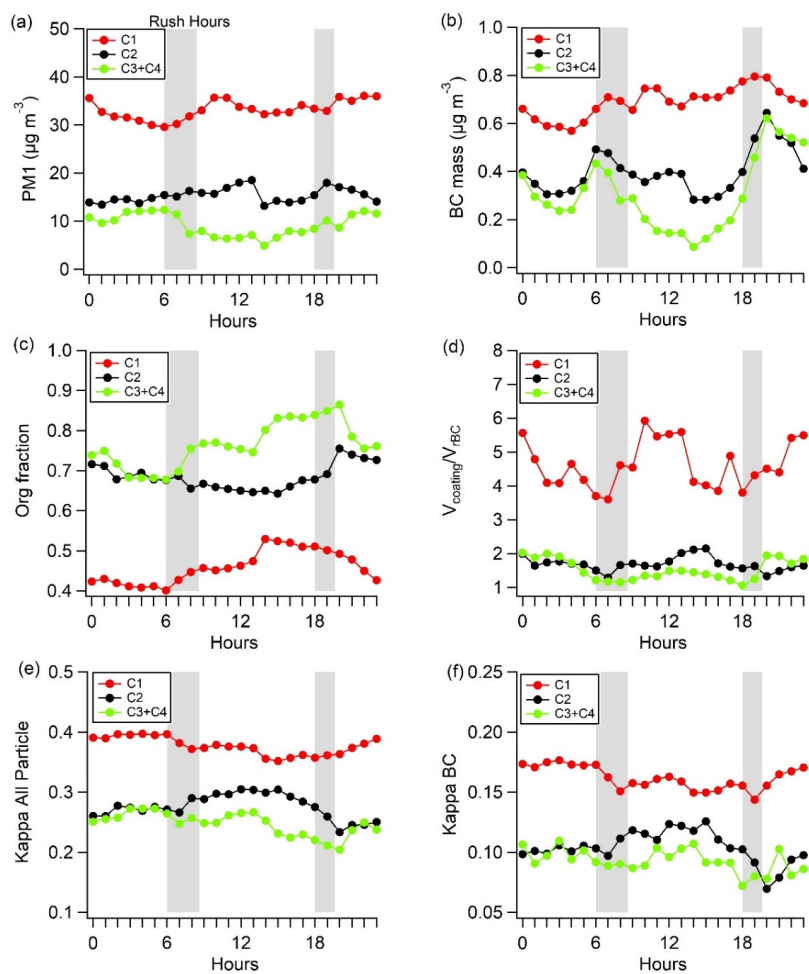
651



652

653 **Figure 2.** Time series of a) mass concentrations for chloride (Chl), ammonium (NH<sub>4</sub>), nitrate (NO<sub>3</sub>), organic  
 654 (Org), sulfate (SO<sub>4</sub><sup>2-</sup>), BC mass and PM<sub>1</sub> measured by HR-TOF-AMS, SP2 and GRIMM. b) Volume fraction of  
 655 particle components for NH<sub>4</sub>HSO<sub>4</sub>, (NH<sub>4</sub>)<sub>2</sub>SO<sub>4</sub>, NH<sub>4</sub>NO<sub>3</sub>, Organic and BC, c) V<sub>coating</sub>/V<sub>BC</sub>, d) κ for all particle and  
 656 BC respectively. The flag on the top of the graph represents different clusters by different colours. Mass  
 657 concentrations of e) Organic fraction and PM<sub>1</sub> by summing HR-ToF-AMS components and BC mass from SP2, f)  
 658 BC mass, g) V<sub>coating</sub>/V<sub>BC</sub>, h) κ, i) t<sub>age</sub> for all particle (red) and BC (black) for four clusters, with solid circle  
 659 indicating the average; in each box, the solid line and top and bottom boundaries represent the median, 75<sup>th</sup> and  
 660 25<sup>th</sup> percentiles, respectively.

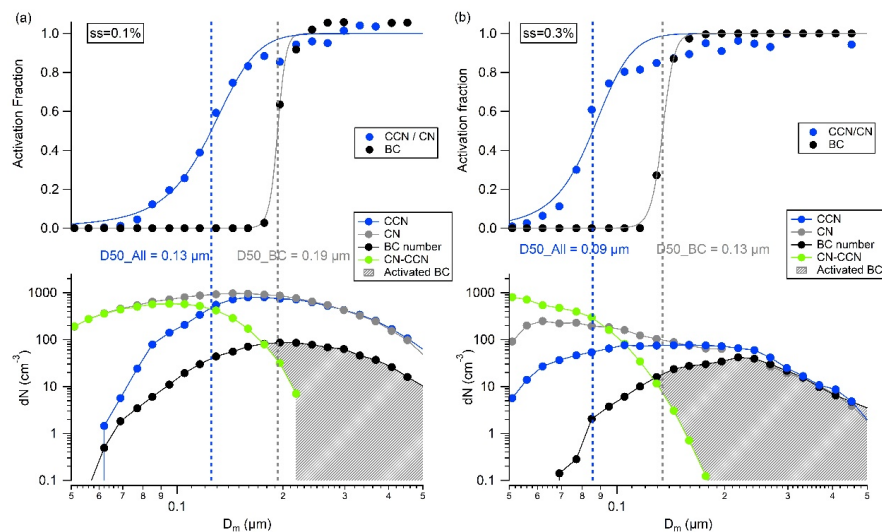
661



662

663 **Figure 3.** Diurnal variations of a)  $PM_{10}$ , b) BC mass, c) Organic fraction, d)  $V_{coating}/V_{BC}$ , e)  $\kappa$  for all particles and f)  
 664  $\kappa$  for BC for four clusters, respectively. Grey bars indicate the traffic rush hours, and the red, black, and green  
 665 line represent the C1, C2 and C3/C4 period, respectively.

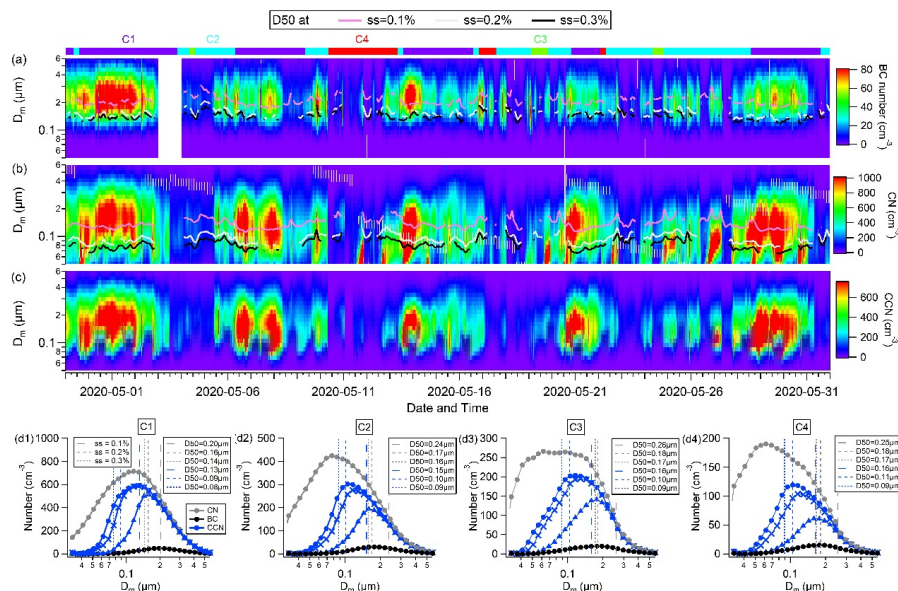
666



667

668 **Figure 4.** A typical example of size-resolved number concentrations of CN, CCN and BCc under supersaturation  
 669 of a) 0.1% and b) 0.3%. The green lines show the un-activated number concentration and the grey shadows  
 670 indicate the activated BCc number concentrations at each size. The blue and black dots in the upper panel show  
 671 the activation fraction of all-particle and BCc. The blue and grey lines indicate the sigmoid fitting on the size-  
 672 resolved activation fraction of all-particle and BC respectively, with the vertical dash lines indicating the  
 673 respective activation diameters.

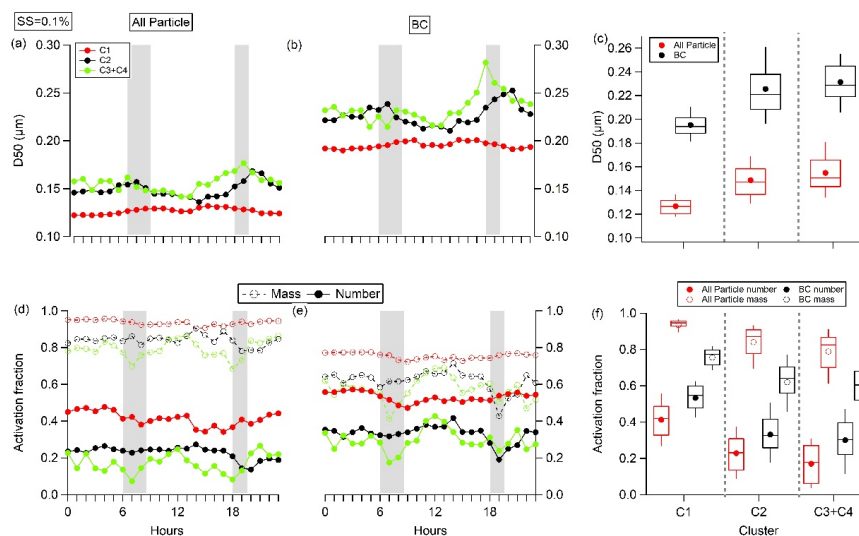
674



675

676 **Figure 5.** Temporal evolution of numbers of a) BCc, b) CN, c) CCN and activation diameter (D50) of BCc and  
 677 CN particles under SS=0.1%, 0.2% and 0.3%. d) Mobility particles size distribution of CN, BCc and CCN  
 678 numbers under SS=0.1%, 0.2% and 0.3% for different clusters. The blue and grey dash lines on the images  
 679 denote the D50 for all-particles and BCc under different SS, respectively. Bottom panels show the mean particles  
 680 size distributions of CN, CCN (under the three SSs) and BCc, for the classified air masses.

681

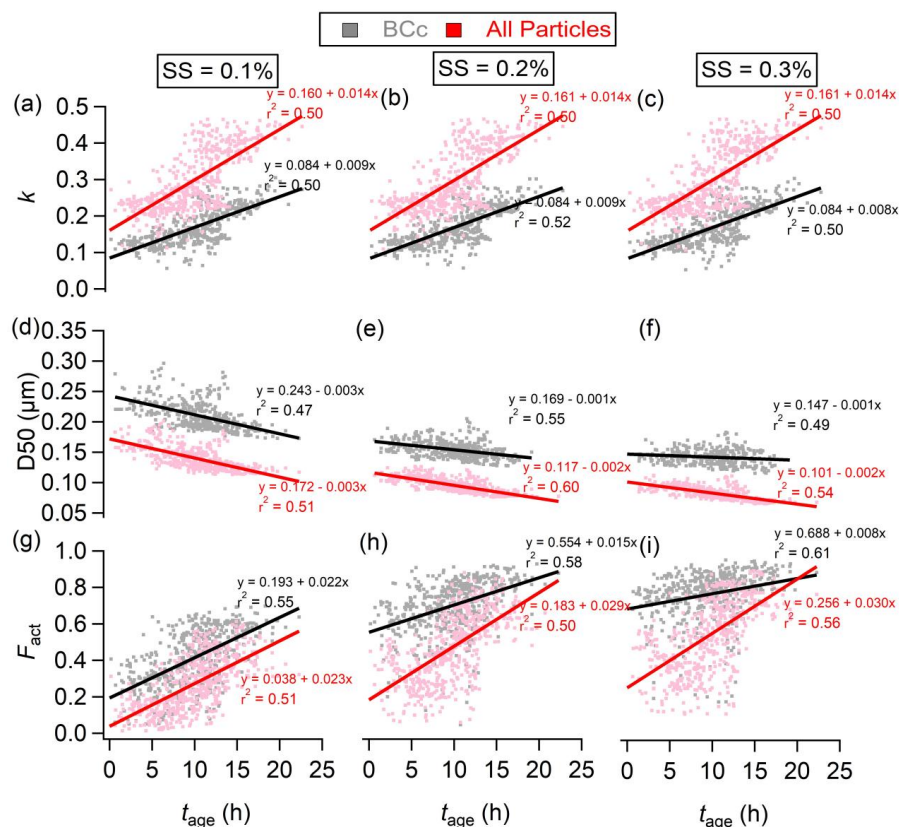


682

683 **Figure 6.** Diurnal variations of D50 of a) all-particles, and b) BCc particles under SS=0.1% for different air mass  
 684 clusters, respectively, c) the statistical of D50 for different air mass cluster, with solid circle indicating the  
 685 average; in each box, the solid line and top and bottom boundaries represent the median, 75<sup>th</sup> and 25<sup>th</sup>,  
 686 respectively. c) diurnal variation of the activation fraction of all-particles, and e) BCc particles, with the solid and  
 687 dash line represent the number and mass fraction, the mass (number) activation fraction was calculated by  
 688 summing the mass (number) of particles with diameter larger than D50, and divided by the total mass (number). f)  
 689 statistical of the activation fraction.

690





691

692 **Figure 7.** The evolution of hygroscopicity parameter ( $\kappa$ ) (a-c), activation diameter ( $D_{50}$ ) (d-f), and number  
 693 activation fraction ( $F_{act}$ ) (g-i) with photochemical age ( $t_{age}$ ) under SS at 0.1%, 0.2%, c) 0.3%. The black and red  
 694 denote the BCc particles and all-particles, respectively. The lines show the least-square linear regression.